Supporting Information

for

Nanomechanical Behavior and Interfacial Deformation Beyond the Elastic Limit in 2D Metal-Organic Framework Nanosheets

Zhixin Zeng[1], Irina S. Flyagina[1,2] and Jin-Chong Tan[1,*]

[1]Multifunctional Materials & Composites (MMC) Laboratory, Department of Engineering Science, University of Oxford, Parks Road, Oxford, OX1 3PJ, UK

[2]A.N. Frumkin Institute of Physical Chemistry and Electrochemistry of the Russian Academy of Sciences, 31 Leninsky prospect, Moscow, 119071, Russia

**E-mail of corresponding author: jin-chong.tan@eng.ox.ac.uk*

Table of Contents

S1. Synthesis of CuBDC Nanosheets and Sample Preparation for AFM Nanoindentation

0.29 g of copper(II) nitrate trihydrate (Sigma-Aldrich) was dissolved in a mixture of 5 mL of *N*, *N*-dimethylformamide (DMF) and 10 mL of acetonitrile in a glass vial with the assistance of ultrasonication. Similarly, equimolar quantity of terephthalic acid (0.2 g, Sigma-Aldrich) was dissolved in a mixture of 10 mL of DMF and 5 mL of acetonitrile. The terephthalic acid solution was placed in a glass test tube. A mixture of 2 mL of DMF and 2 mL of acetonitrile was added on the top of the terephthalic acid layer dropwise to create a separation layer. The copper(II) terephthalate solution was added slowly dropwise as a third layer. The test tube was left in an oven at 40 °C overnight. As a result of the Cu^{2+} ions diffusion to the bottom layer and interaction with terephthalic acid, the CuBDC nanosheet crystals were formed. The CuBDC crystals were centrifuged and washed with DMF three times and then methanol three times with ultrasonication. The exfoliated nanosheets for AFM nanoindentation were further diluted using methanol and then drop-casted onto a silicon wafer. Note that the more diluted the solution is and the steeper the substrate is held inclined while drop casting, the better dispersed the nanosheets are. Thereafter, the sample deposited on substrate was dried in a vacuum oven at 40 °C overnight and transferred to a desiccator for storage before nanoindentation tests.

The bulk of the nanosheets for XRD characterization was dried in a vacuum oven at 40 °C overnight. The material yield of CuBDC was determined to be ~18 wt.% (a fractional amount of solvent may remain in the pores, and thus introducing deviations), this relatively low yield is in agreement with ref 1.

S2. Characterisation of the Geometry of the Cube-Corner Indenter Tip

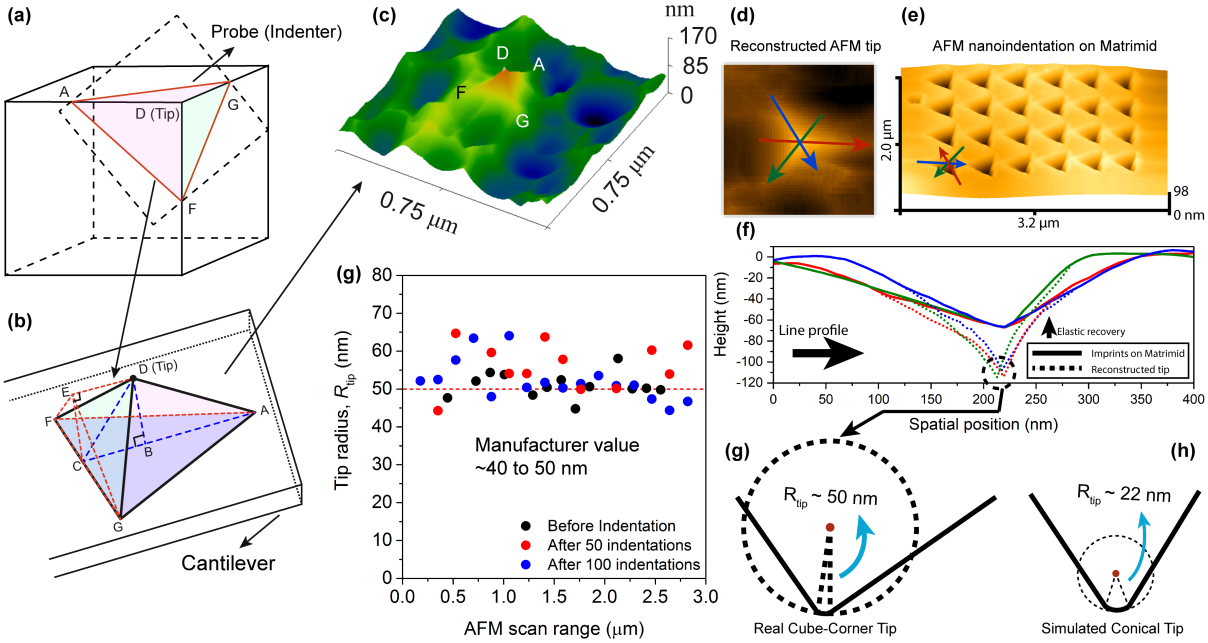

Figure S1. (a-b) Schematics of a cube-corner indenter, which can be used to implement both AFM imaging and nanoindentation.[2] (c-d) Height topographic images (in two distinguishable modes of colour map) of the indenter tip geometry reconstructed *via* the Villarrubia algorithm.[3] (e) Residual indents generated by the indenter after unloading, and (f-g) the corresponding line profiles indicating the radius of the diamond indenter apex (r ~50 nm) acquired by the Villarrubia algorithm. (h) the simulated equivalent conical indenter tip of a curved apex (r ~22 nm) Adapted with permission from ref 2. Copyright (2017) American Chemical Society.

The Villarrubia blind estimation algorithm[3, 4] was adopted to reconstruct the geometry of the indenter tip due to the fact that the indenter could be worn/abraded over a period of time leading to the change of contact area at a certain depth. The algorithm was implemented in the Gwyddion software.[5] By means of the algorithm, it was confirmed as shown in Figure S1g that the geometry of the diamond indenter has been consistently intact even after performing more than 200 indentations on relatively soft materials (Young's moduli of the samples tested in this study are < 50 GPa). Table S1 shows the dimensions estimated for the cube-corner indenter tip, with which the nominal contact area as a function of the indentation depth, $A(h)$, can be determined.

Table S1. Dimensions of the diamond cube-corner indenter tip: (left) included angles and (right) side lengths at the indentation depth h_{DB} = 50 μm, they were derived by applying the Pythagorean theorem.

Angles of the indenter				At indentation depth (μm) h_{DB} = 50	
	*1	*2			
Front angle $\angle_{ADB}$	55 ± 2°	58.2422°		Side length L_{AB}	71.4074
Back angle $\angle_{CDB}$	35 ± 2°	35.1542°		Side length L_{CB}	35.0104
Side angle $\angle_{CEF}$	51 ± 2°	49.1985°		Side length L_{FC} (L_{GC})	61.7449
Equivalent conical angle (2θ)*		91.4667°		Side length L_{AG} (L_{AF})	123.0332

*1: The manufacturer's specifications

*2: The real-time included angles of the cube-corner tip reconstructed by applying the Villarrubia algorithm.

*: An equivalent conical indenter tip of the included angle is 2θ, which has the same surface area as the cube-corner indenter tip (see the concept of "effective indenter shape" in ref 6).

S3. Characterisation of the CuBDC Nanosheets and Residual Indents from the AFM Nanoindentation Measurements

Figures S2-S5 show the residual indents present on the surface of the nanosheet specimens after being probed using a cube-corner indenter tip. The CuBDC nanosheets exhibit differential deformation behaviour, reflected by the resulting *P-h* curves in Figure 5f of the main body of the paper. The different loading forces and the irregular nature of contacts between the indenter tip and specimen may be attributed to the packing of the CuBDC nanosheets and microstructural defects (e.g. Figure S5).

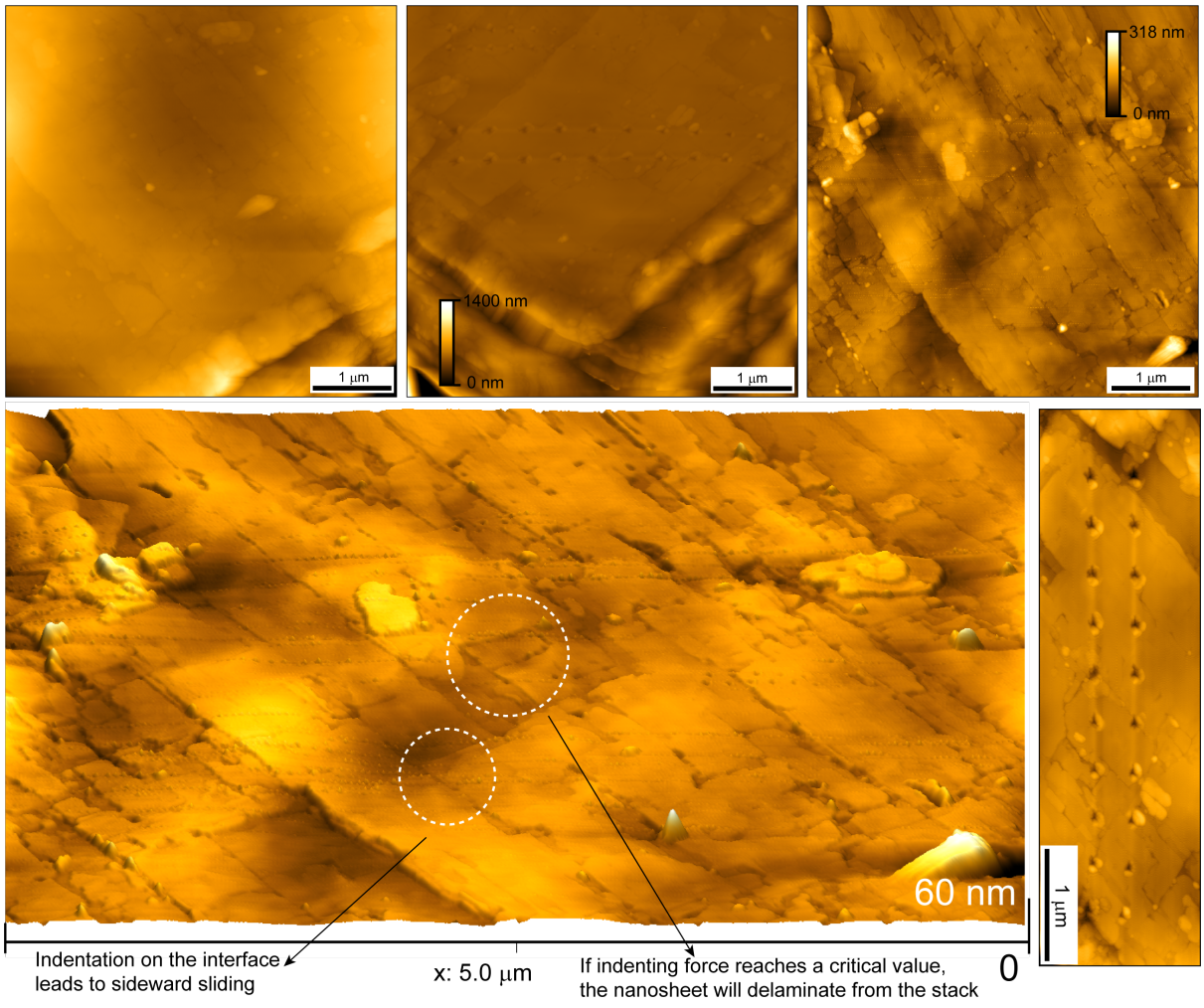

Figure S2. AFM topographic images of stacks of fragmented CuBDC nanosheets. Two columns of the residual indents created by a cube-corner indenter are shown in the bottom right panel.

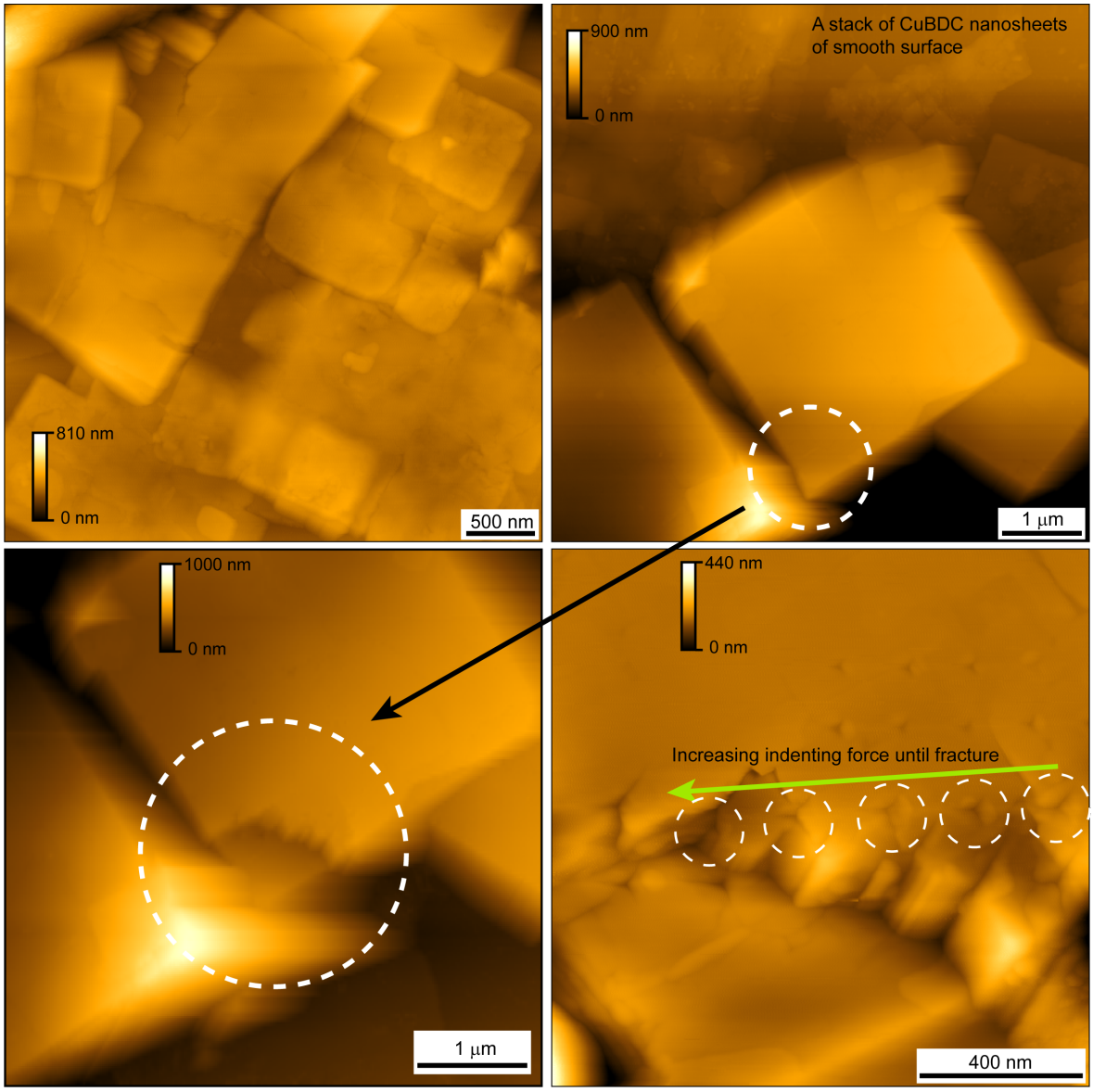

Figure S3. AFM topographic images of stacks of CuBDC nanosheets with smoother surface compared with the ones shown in Figure S2 since for the purpose of accurate characterization of mechanical properties, such as *E* and *H*, the cracks or local defects should be avoided to indent. The fracture of a CuBDC nanosheet is displayed in the bottom right panel.

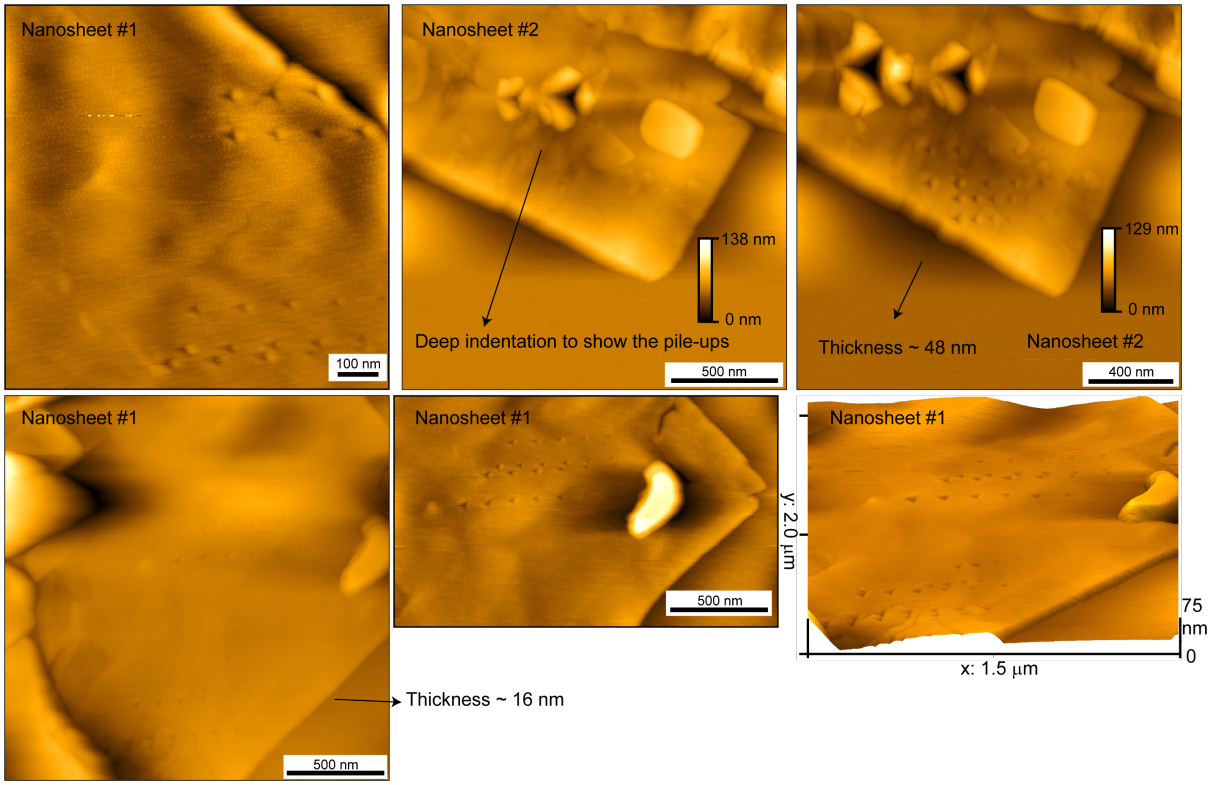

Figure S4. AFM images of two thin CuBDC nanosheets (sample #1 is thinner than #2), of which the severe indentation substrate effect takes effect (exceeding the recommended 10% rule of the nanosheet thickness).

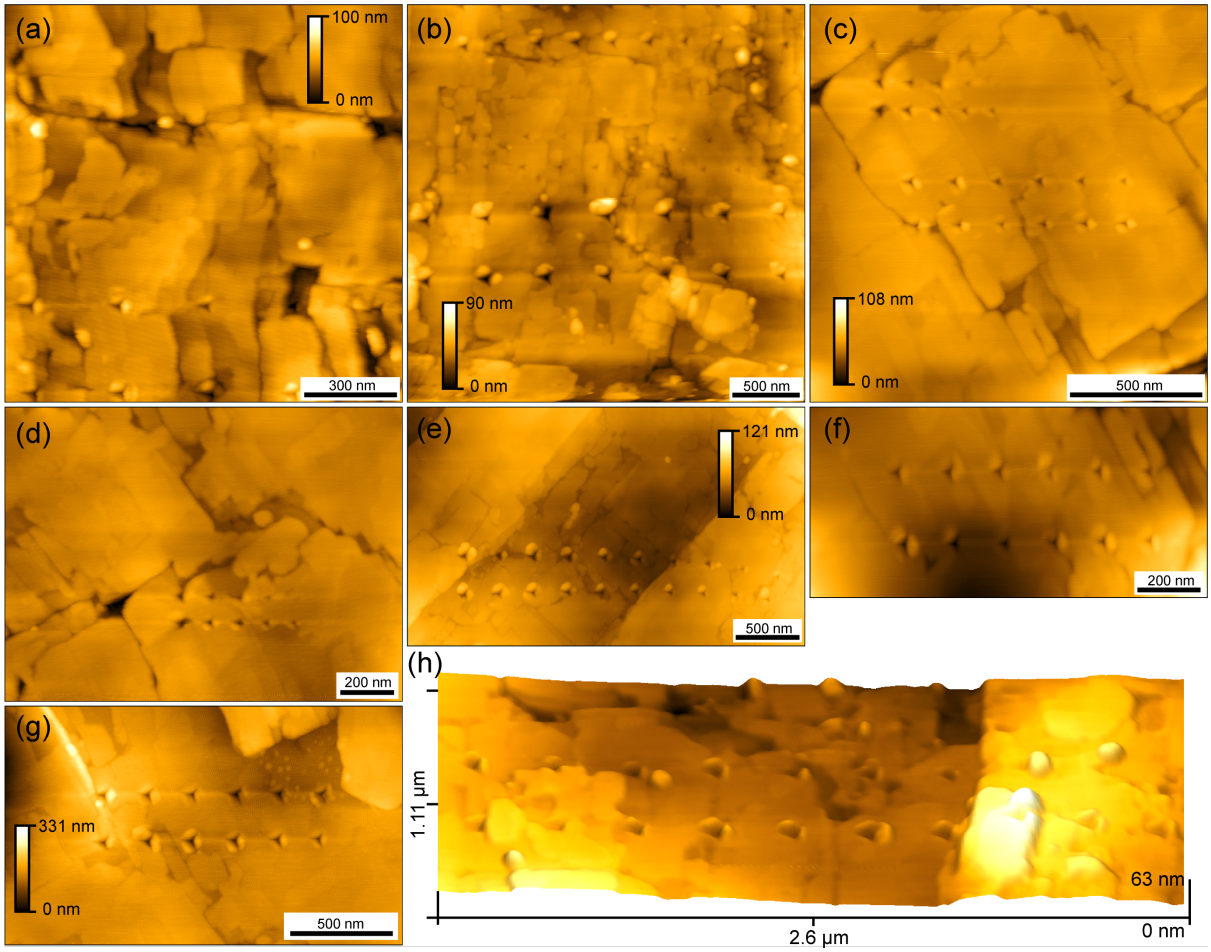

Figure S5. (a-g) AFM topographic images of stacks of CuBDC nanosheets, on which the residual indents can be observed. AFM nanoindentation equipped with the cube-corner indenter was applied to the specific sites of the stacks to identify the failure modes. (h) A 3-D height image of the AFM nanoindentation experiments on a CuBDC nanosheet stack.

S4. The Height of the Pile-Ups Produced by Indenting on CuBDC using the Cube-Corner Indenter

Table S2. The ratio (*s/h*) of the height of a residual pile-up (*s*) to the indention depth (*h*) of the pile-ups (pile-ups on the three sides of a residual indent are illustrated in Figure S6). Note that for some indents produced by the cube-corner indenter on the nanosheet stacks, there were pile ups on only one or two sides (probably because of structural anisotropy of the underlying 2D framework), to which the zero values in the table are ascribed. It is necessary to mention that considerable standard deviation of the pile up height implies that the values of hardness and yield stress are of a certain level of uncertainties.

s/h		
Pile-up Back	**Pile-up Left Side**	**Pile-up Right Side**
0.07231	0.05984	0.10518
0.09783	0.09395	0.14726
0.05209	0.21101	0.06862
0.08015	0.11748	0.13084
0.04578	0.05602	0.08195
0.05057	0.08526	0.14407
0.07009	0.04258	0.12177
0.03106	0.14186	0.11498
0.02553	0.24621	0.11707
0.04715	0.00000	0.07270
0.03021	0.00000	0.09536
0.05085	0.00000	0.10523
0.05314	0.00000	0.08961
0.05737	0.00000	0.11113
0.11416	0.00000	0.08008
0.16024	0.00000	0.11598
0.14629	0.00000	0.13464
0.20887	0.00000	0.05957
0.17102	0.00000	0.07836
0.06580	0.00000	0.07039
0.11675	0.00000	0.15866
0.16534	0.00000	0.00000
0.15110	0.00000	0.00000
0.20377	0.00000	0.00000

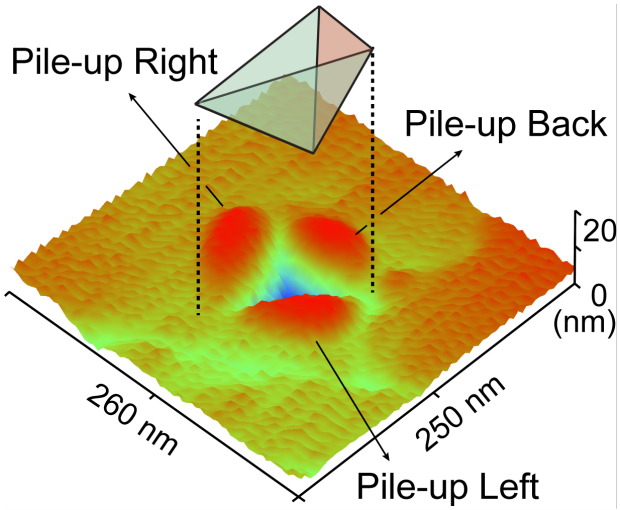

Figure S6. Schematic illustration of a residual pile-up

	Pile-up Back	**Pile-up Left Side**	**Pile-up Right Side**	**Mean of the *s/h* ratio of all the pile-ups**
Mean*	0.09448	0.11713	0.10493	0.10551
Standard Deviation*	0.05724	0.07090	0.02850	

* The values were obtained by only considering the non-zero values of the pile-up height.

S5. Finite-Element Model of Indentation (No Material Failure)

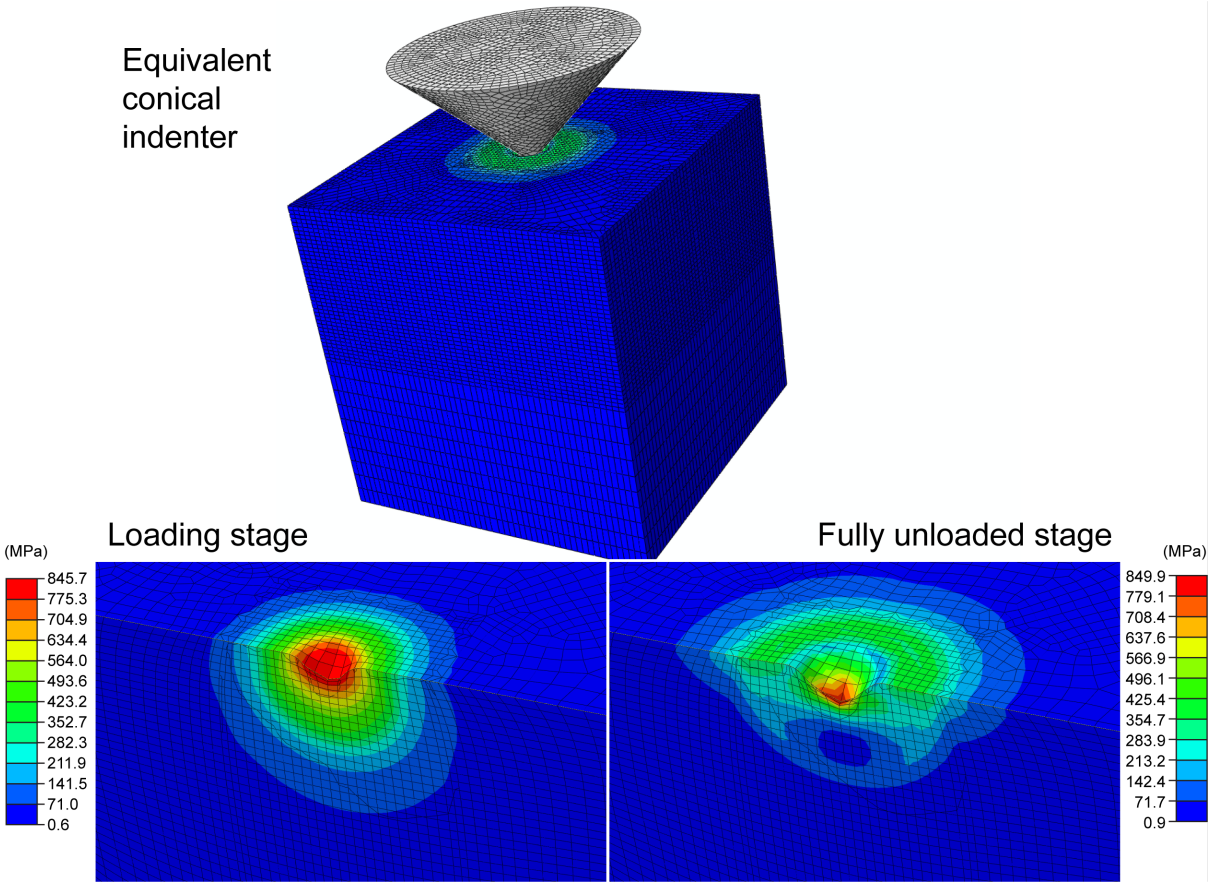

Figure S7. The FE model with the von Mises stress contour showing the indentation using an equivalent conical indenter (same contact area over depth as the cube-corner indenter, see the "effective indenter shape" in Table S1) on a continuum model of CuBDC (the von Mises stress contour plot, same as the ones shown in Figure 4e-f). The input material properties include elasticity (acquired from the AFM nanoindentation experiment) and plasticity (obtained from the mathematical iteration method shown in Figure 4d of the main body of the paper).

In order to avoid the influence of mesh on the resulting value of the *s/h* ratio, the mesh convergence study was conducted as shown in Figure S8.

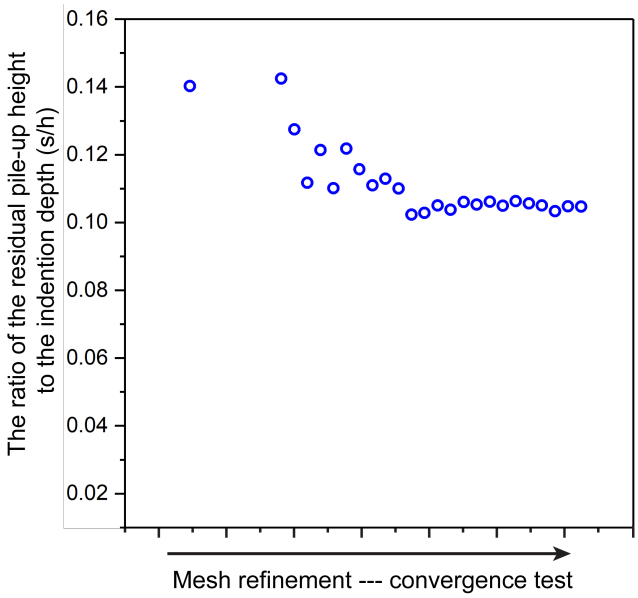

Figure S8. Mesh convergence plot showing that the mesh system is sufficiently fine so that the result of *s/h* is independent of the mesh size.

Table S3. Materials parameters used for the FE model.

Elastic Behaviour		**Plastic Behaviour**	
Young's Modulus	Poisson's Ratio	Yield Stress	Plastic Strain
22.9 GPa	0.4	448 MPa	0
From AFM Nanoindentation	Assumption (please see Figure S11)	From the iterative method: $\sigma_y = 863.521 \cdot {\varepsilon_p}^{0.173}$	

S6. Finite-Element Model of the Indentation which Causes Interfacial Sliding Failure and Delamination Failure

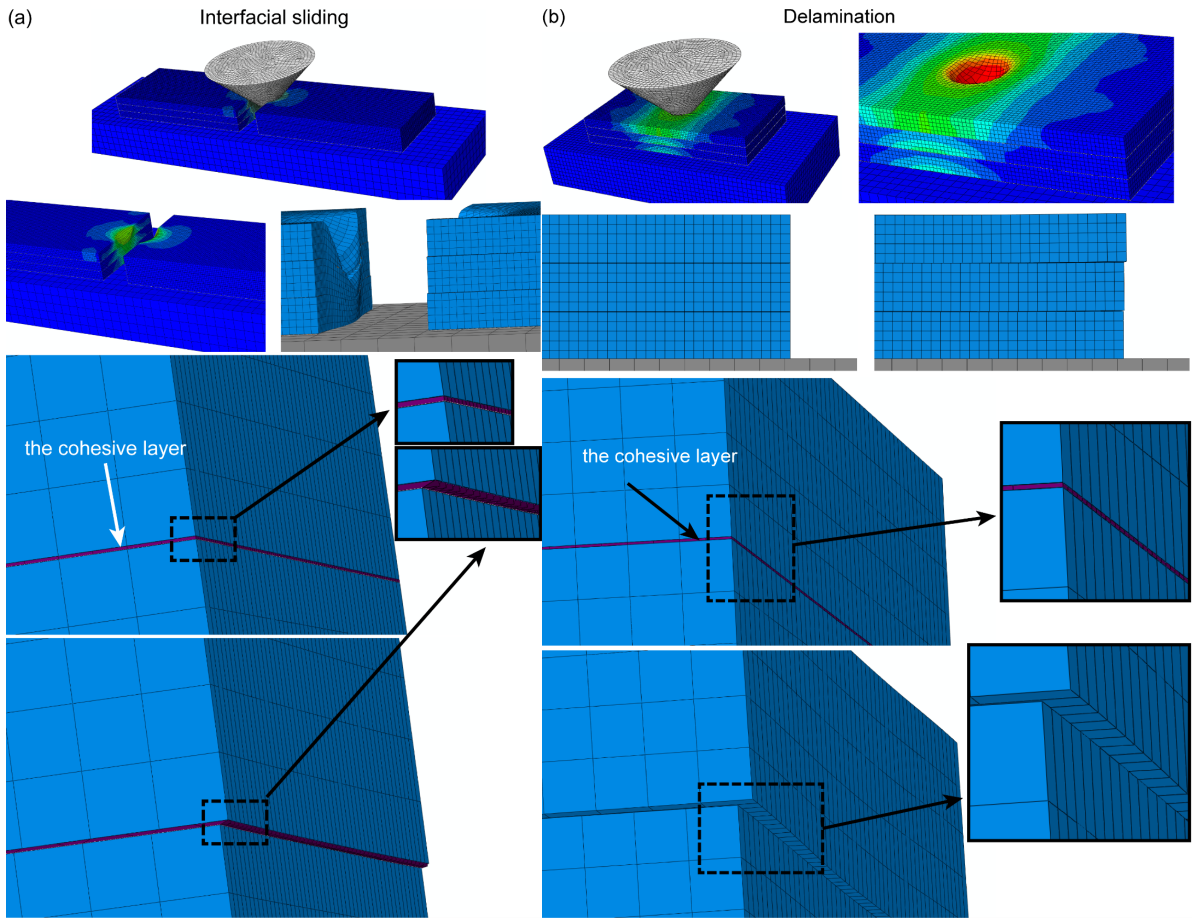

Figure S9. The FE model with the von Mises stress contour showing (a) the sideward/interfacial sliding and (b) the delamination caused by the penetration of the indenter (the cohesive layers are shown in purple).

The cohesive layer represents the bonded interaction between the adjacent nanosheets. In the FE model, the cohesive layer was modelled as a thin sheet of 1% thickness of the CuBDC monolayer model. Separation of the layer occurs when the displacement reaches a designated threshold value. The cohesive layer in the FE model follows a linear traction-separation response. In the CuBDC nanosheet model, the cohesive layer starts to "degrade" (or fail) when the maximum nominal stress reaches a threshold value in either the normal or shear directions. By adopting this approach in conjunction with AFM nanoindentation experiments, both interfacial sliding (in the shear direction) and delamination (in the normal direction) can be investigated.

As shown in Figure 5 in the main body of the paper, the FE models simulating the three failure modes were not quantitative but were created to verify the distinct distortion patterns of the *P-h* curve when different failure modes occurred in the nanosheets. Although the specifications of the damage criteria of the cohesive layer and the fracture model are summarized in Table S4, the absolute values in the table do not necessarily corresponding to the actual values when failure occurs in the CuBDC nanosheets.

Table S4. Dimensionless parameters of the maximum nominal stress criterion (Maxs Damage) and the Johnson-Cook damage criterion. Note that the values presented herein are not the absolute mechanical properties of the CuBDC nanosheets and refer to ref 7 for further details regarding the parameters in the table.

Cohesive layer		**Fracture Model**	
Maxs Damage	Values	Johnson-Cook Damage	Values
Tolerance	0.05	Failure Parameters: d_1, d_2, d_3, d_4, d_5	-1, 1.1, 0.4, 0.001, 0
Nominal Stress Normal-Only Mode	0.0001	Melting Temperature	0
Nominal Stress First Direction	0.0001	Transition Temperature	0
Nominal Stress Second Direction	0.0001	Reference Strain Rate	1
Damage Evolution – Displacement	Degradation: Maximum; Displacement at Failure: 0.0002	Damage Evolution – Displacement	Degradation: Maximum; Displacement at Failure: 1.0E-007
Damage Stabilization Cohesive	Viscosity Coefficient: 1.0E-006		
Mass Density	8.6E-010	Plastic – Johnson-Cook Hardening	A = 300; B = 110; n = 0.4; m = 1; Melting Temperature = 0; Transition Temperature = 0.
Elastic – Traction	E/E_{nn} = 1000; $G1/E_{ss}$ = 1000; $G2/E_{tt}$ = 1000.	Rate Dependent	C = 0.003; $\dot{\varepsilon}_0$= 1.

S7. Finite-Element Model of the Indentation which Causes Fracture Failure

The plasticity model shown in Figure S10 was built based on the Johnson-Cook hardening model, the static yield stress (σ^0) of which is given by:[8]

$$\sigma^0 = [C_1 + C_2(\bar{\varepsilon}^{pl})^n]\left(1 + C_3 ln\frac{\dot{\varepsilon}}{\dot{\varepsilon}_0}\right)[1 - (T^*)^m] \quad \text{(S1)}$$

where $\bar{\varepsilon}^{pl}$ is the equivalent plastic strain and C_1, C_2, m, n are material parameters that can be derived from the experiment. $\dot{\varepsilon}$ and $\dot{\varepsilon}_0$ are the current and reference strain rate, respectively. T^* is the temperature constant that is defined as $T^* = \frac{T-T_t}{T_m-T_t}$, where T_t and T_m are the material transition and melting temperatures, respectively.[8, 9] If the current temperature $T \leq T_t$, the mathematical expression of σ_0 is independent of temperature, i.e. $T^* \equiv 0$ (assumption in the FE model). Determination of these parameters normally requires a series of quasi-static and dynamic tests, such as tensile test with high triaxiality.[9] However, it is practically impossible to implement these tests on the nanoscale CuBDC nanosheets. Therefore, in this work, the fracture model of CuBDC nanosheets being implemented was aimed at gaining a semi-quantitative insight into which part of the *P-h* curve distortion that can be linked to the fracture of materials.

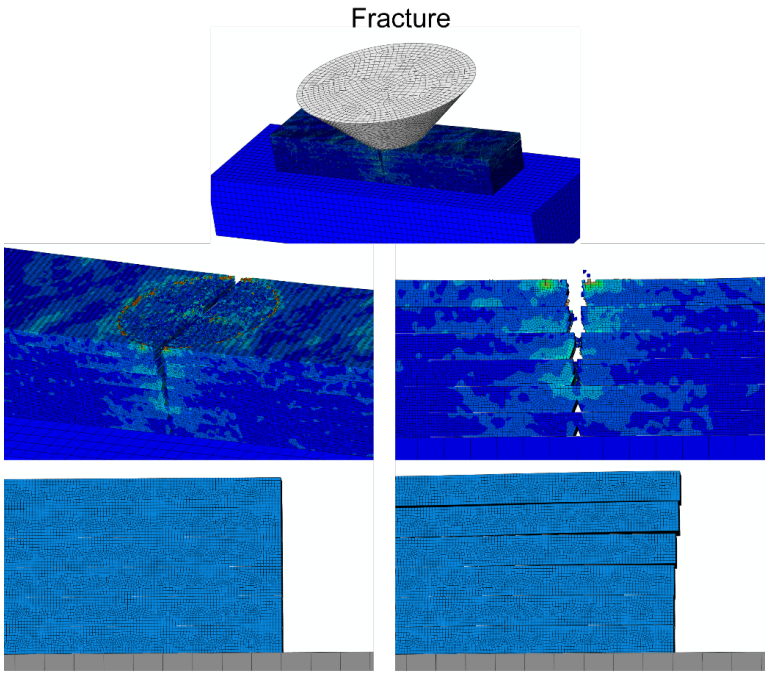

Figure S10. The FE model with the von Mises stress contour showing the fracture of the CuBDC nanosheets caused by stress concentration (the von Mises stress contour plot) induced by the sharp indenter tip.

S8. Young's Modulus vs Unloading Strain Rate with Varying Poisson's Ratio

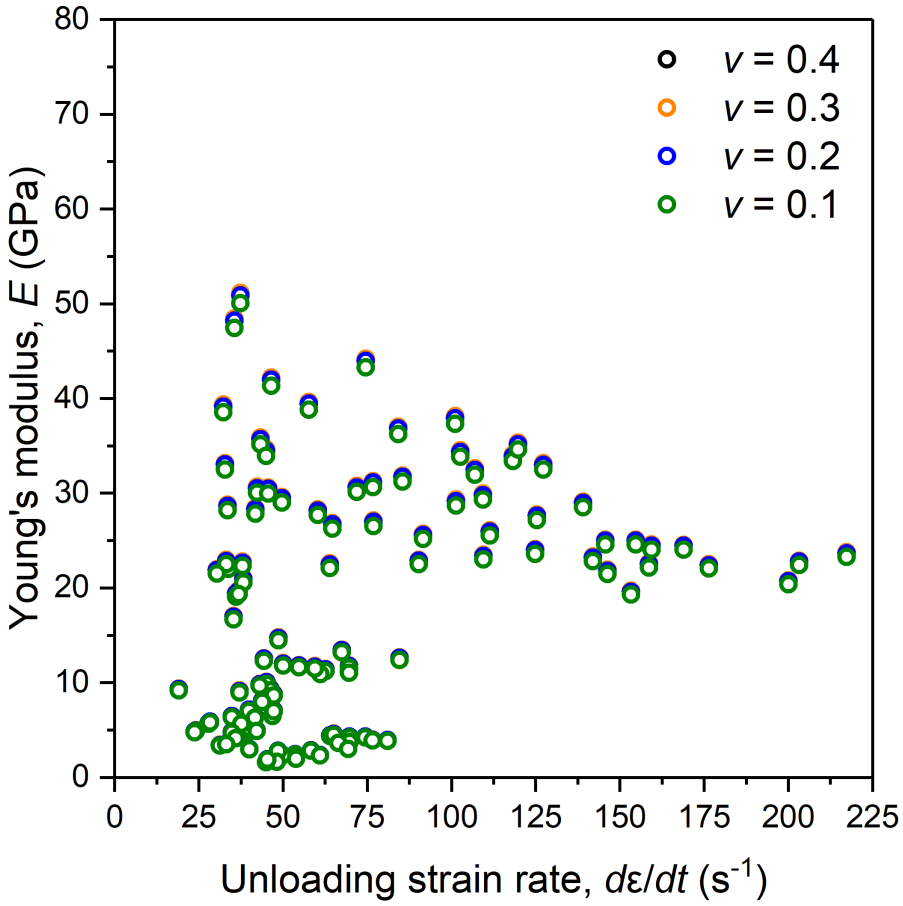

Figure S11. Young's modulus (E) versus unloading strain rate plot assuming v = 0.1, 0.2, 0.3, 0.4 to demonstrate the negligible influence of v on E.

S9. Hardness vs Indentation Depth with Yield Stress Indicated

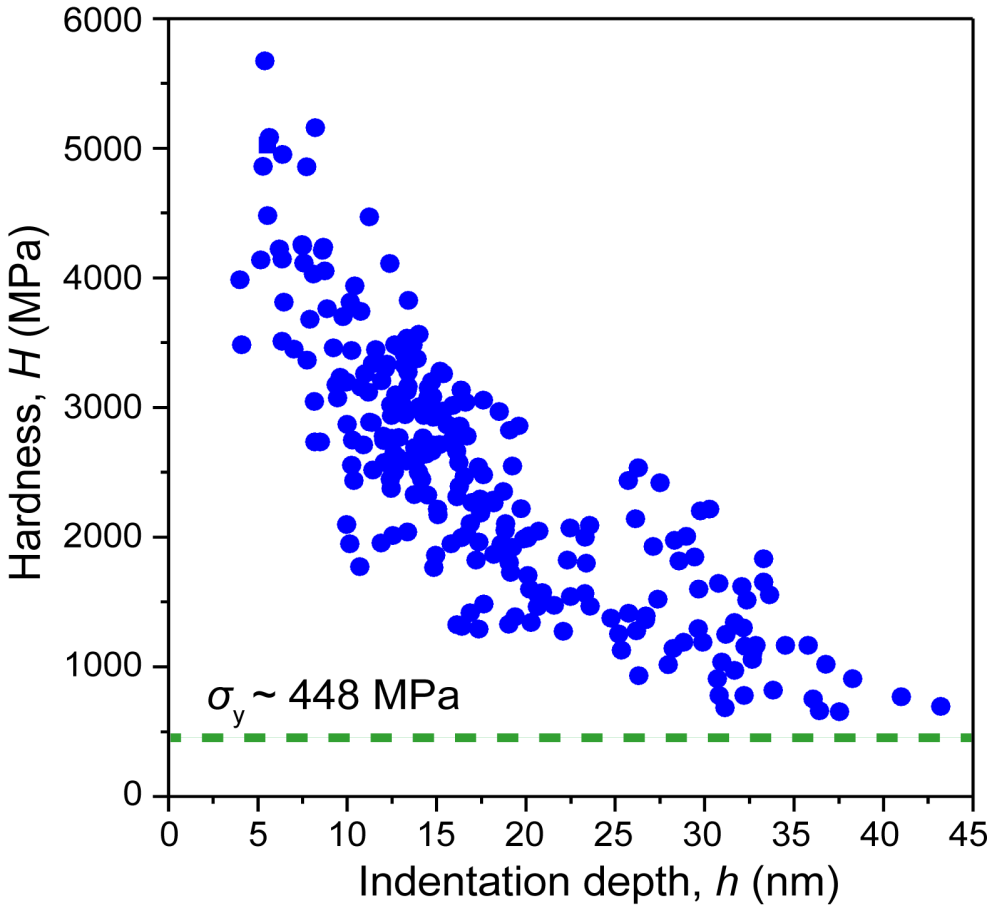

Figure S12. Hardness plotted as a function of the indentation depth; the value of the yield stress of the CuBDC nanosheets is approximated by the dashed line.

S10. Threshold Forces and Displacements Resulting in Different Failure Modes

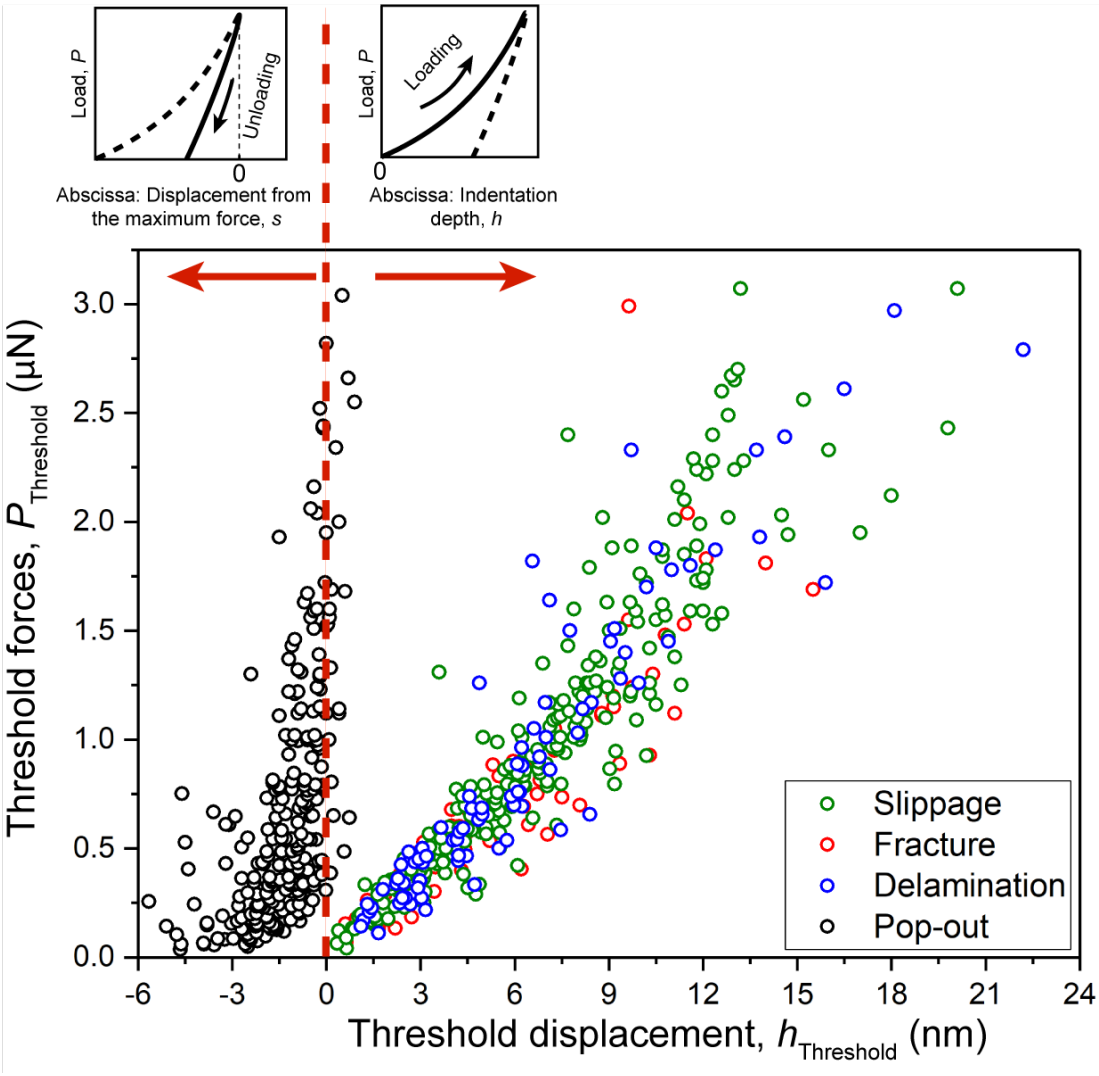

Figure S13. The threshold forces resulting in the three failure modes during the loading stage as the function of the threshold depths; and the threshold forces leading to the pop-out phenomenon as a function of the displacement from the maximum force during the unloading stage (because it is in the opposite direction, the displacement has a negative value). Note that a small portion of the data points for the pop out are positive due to the distortion of the incipient unloading curves.

S11. Identification of the Threshold Forces and Indentation Depths

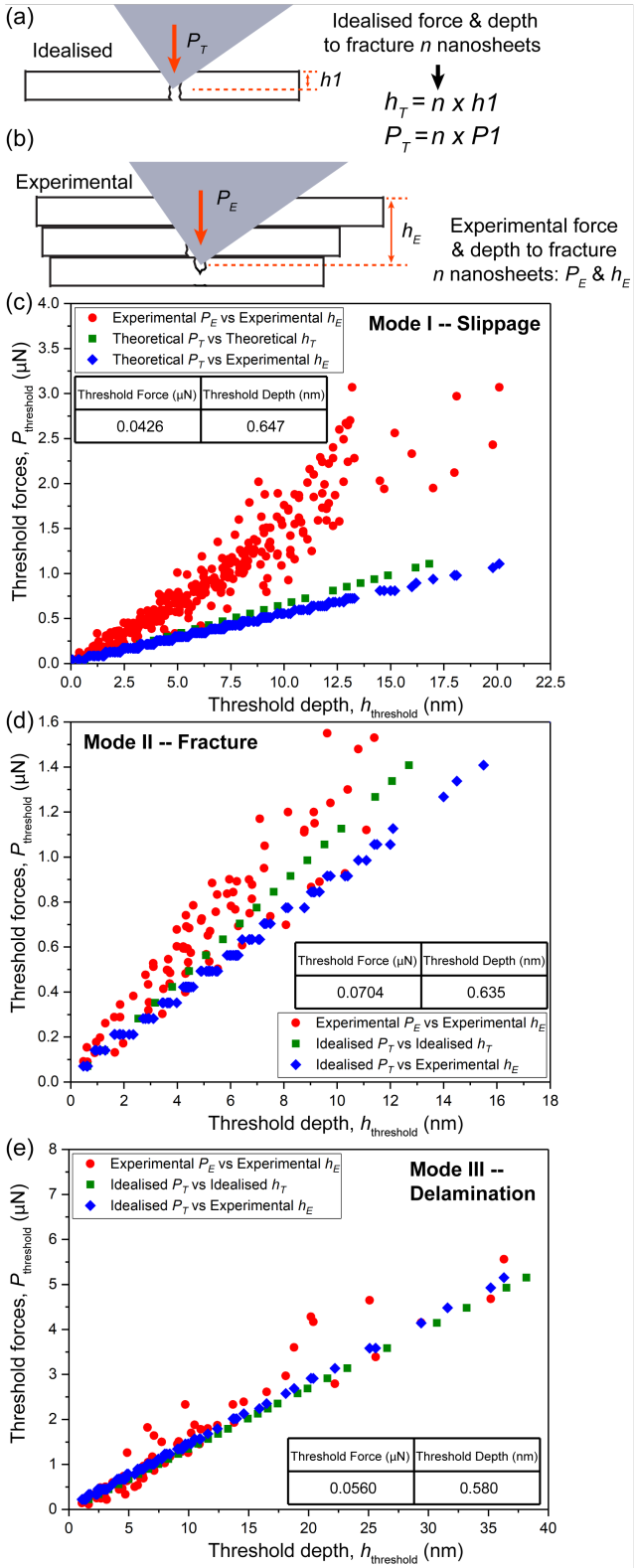

Figure S14. Schematic illustrations of the (a) idealised (i.e. analytically modelled) and (b) experimental forces and depths, respectively. Comparison between the idealised and experimental data in the plot of threshold forces as a function of threshold depth in regard to these failure modes: (e) Mode I – slippage, (f) Mode II – fracture, (g) Mode III – delamination.

An ideal scenario that the area of the stress field stays constant with increasing penetration depth, hence the idealised threshold forces and threshold depths triggering the failure modes can be estimated. The idealised force and depth are obtained by proportionally increasing the unit idealised force (the force leading to the failure of a monolayer) and corresponding unit indentation depth that cause any one of the three aforementioned failure modes. And this forms the data points (in blue and green in Figure S14c-e) that are linearly distributed. It was found that only the data points based on the genuine unit force and unit depth (thickness $t \sim 0.5$ nm, see Figure 1a in the main body of the paper) are able to define the lower bound of the experimental data points (red in Figure S14c-e). However, in reality, as the cube-corner indenter continues to penetrate into the material, the stress spreads constantly thus the affected area is continuously growing. As illustrated in Figure 6 in the main body of the paper, a higher force is needed to overcome the counter-acting force from the cohesive layer, whose area increases rapidly with the stress spreading. Therefore, the experimental threshold forces causing the interfacial sliding spread more rapidly (see Figure S14c) and hence increasing at a higher speed than the idealised values by contrast with fracture (Figure S14d) and delamination (Figure S14e).

References

1. C. G. Carson, K. Hardcastle, J. Schwartz, X. Liu, C. Hoffmann, R. A. Gerhardt and R. Tannenbaum, *Eur. J. Inorg. Chem.*, 2009, **2009**, 2338-2343.
2. Z. Zeng and J. C. Tan, *ACS Appl. Mater. Interfaces*, 2017, **9**, 39839-39854.
3. J. S. Villarrubia, *J. Res. Natl. Inst. Stand. Technol.*, 1997, **102**, 425-454.
4. L. S. Dongmo, J. S. Villarrubia, S. N. Jones, T. B. Renegar, M. T. Postek and J. F. Song, *Ultramicroscopy*, 2000, **85**, 141-153.
5. D. Nečas and P. Klapetek, *Cent. Eur. J. Phys.*, 2012, **10**, 181-188.
6. W. C. Oliver and G. M. Pharr, *J. Mater. Res.*, 2004, **19**, 3-20.
7. K. S. Hibbitt, Inc., Abaqus Analysis User's Guide, Hibbitt, Karlsson & Sorensen, Inc.: Pawtucket, RI, USA, 2016.
8. G. R. Johnson and W. H. Cook, *Eng. Fract. Mech.*, 1985, **21**, 31-48.
9. G. H. Majzoobi and F. R. Dehgolan, *Procedia Eng.*, 2011, **10**, 764-773.